Journal of Engineering Science and Technology
Vol. 16, No. 4 (2021) 2795 - 2815

AUTONOMOUS TRACKING AND LANDING ON MOVING GROUND VEHICLE WITH MULTI-ROTOR UAV

SWEE KING PHANG[1,*], XUDONG CHEN[2]

[1]Taylor's University, 1 Jalan Taylor's, 47500, Subang Jaya, Selangor DE, Malaysia
[2]The Robotics Institute, School of Computer Science, Carnegie Mellon University, Pittsburgh, PA. 15213, USA
[*]Corresponding Author: sweeking.phang@taylors.edu.my

Abstract

In this manuscript, an autonomous system to track a moving ground vehicle and landing on it with multi-rotor UAV is proposed. Technical development of such system is discussed in detail. It includes sensors selection and integration, target detection algorithm and implementation, mathematical model of UAV and flight controller design. The system utilized near infrared camera which is able to detect the marker even at night or low illuminance, up to 18 Hz with processor on-board UAV. The complete system was first simulated in MATLAB, and then implemented to an actual UAV. The successful flight trials with a small size quad-rotor UAV landing autonomously on a moving small truck have shown that the design is valid and viable to actual applications. The proposed vision-laser target tracking performance has achieved a 99.2% success rate with a static marker, and a 94.4% success rate with a moving marker.

Keywords: Unmanned systems, Target following, UAV flight control.

1. Introduction

In the recent years, many industries have been utilizing Unmanned Aerial Vehicles (UAVs) for specific applications, for example: surveillance, agriculture, disaster rescue and response. Along with the readiness of relevant technologies, UAV is gradually becoming more intelligent and reliable [1, 2]. However, certain tasks remain challenging due to the complicated environmental issues as well as unforeseen operational circumstances. To facilitate the landing of the UAV, global positioning system (GPS), LiDAR and other proximity sensors have been widely used for estimating relative distance between UAV and the landing area. Kendoul [3] has done a fairly comprehensive review that is focusing on the control and navigation of many commonly available UAVs. Landing is always one of the most dangerous phases of the flight and even for the manned aircraft, it requires high concentration and skill to prepare for any unexpected situations [4]. Moreover, due to the limited flight endurance of most quad-copters, the frequent autonomous landing and taking off is highly required to replace battery or refuel in the middle of mission execution.

To date, most researchers have been using GPS-based methods for precise guidance during the landing stage, as documented in [5-8]. Besides utilizing GPS signals, many autonomous recovery systems use millimetre-wave radar with transponders to transmit data onto the UAV that is located on the platform for pose estimation of the UAV. The major drawback of such setup is the extra requirement of sensors on the pre-defined landing spot. On top of that, the communication link between the UAV and the ground station needs to be maintained to facilitate the smooth and safe landing. To solve the issue of communication robustness, [9] and [10] proposed using onboard camera and LiDAR sensor to provide necessary information for the UAV for the landing.

Camera can provide rich information of the surrounding. This results in the rich development of visual-based algorithm for navigation purposes [11, 12]. Based on the investigation on relevant literature, some mono and stereo vision-based methods have been developed, as documented in [13-17]. One biggest challenge in vision-based navigation system is to estimate the velocity of the UAV [18]. Many researchers, for example, documented in [19, 20], proposed to use optical flow to provide linear velocity measurement based on flow estimation. The optical flow algorithm, however, will fail if flat ground assumption does not meet and the objects in the scene are generally static. It is non-trivial to accurately estimate the height in order to achieve smooth touchdown with a rate-based controller. Furthermore, most system are designed with assumption that the lighting condition and environment is always favourable for RGB camera to capture clear images. However, in the real-world applications, some missions are generally executed during the night. Hence, it is a crucial requirement for the UAV to operate in the low light or even totally dark environment to facilitate such requirement.

In this manuscript, inspired by the mentioned consideration, a solution is proposed to facilitate autonomous landing on moving vehicle in both day and nighttime. An infrared (IR) camera is employed to accurately track the pre-defined marker to estimate the horizontal and vertical relative position of the target in the image coordinate system. Meanwhile, a 2D LiDAR sensor is equipped to estimate the flying height. For the system to work more robustly, the height measurement estimated by using the LiDAR sensor will be utilized to effectively filter off high

frequency noise that was introduced by the vision algorithm. An infrared-LED lightened pre-defined marker is mounted on the moving vehicle to indicate the landing spot.

This paper has the following sections: Section 2 will briefly introduce the hardware including sensors, processors and UAV platform. Section 3 focuses on the mathematical model identification of the UAV. Section 4 introduces the linearization approach on the UAV dynamics for application of linear flight controllers. Section 5 illustrates the detection algorithms to robustly track the IR marker. Furthermore, Section 6 show the simulation as well as flight trials results and its discussions. In the last section, concluding remarks will be made.

2. Hardware Design

We utilized a quad-rotor UAV model to realize the proposed algorithm. The platform is fully self-customized, as shown in Fig. 1, with the codename T-Lion. It was developed by the Control Science Group of Temasek Laboratories at the National University of Singapore (TL@NUS). It was specially designed to carry up to 2 kg payload and with the ability to fly for 20 mins. The optimal take-off weight of T-Lion is 5.5 kg, and the tip-to-tip length is 110 cm. The structure of the hardware connection and power distribution is shown in Fig. 2. The detailed design requirement and consideration of the UAV will be illustrated in the following subsections.

Fig. 1. UAV platform codenamed T-Lion.

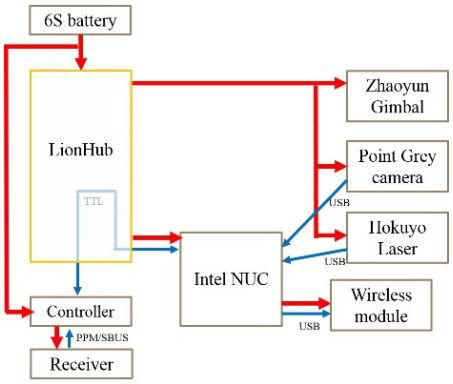

Fig. 2. Hardware connection and data flow of onboard electronics.

2.1. Flight controller

An in-house developed flight controller, as shown in Fig. 3 is equipped on T-Lion to facilitate the flight control. The flight controller is largely inspired by the PIXHAWK [21] flight controller. It consists of two inertial measurement units (IMUs) of different model with an intelligent switch to change primary sensor in case of fault detected on the sensor. The raw measurement data of accelerations and angular rates are fed into a Kalman filter in the flight controller for further processing. A power distribution board is equipped to outputs 12 v, 5 v and 3.3 v for the avionics and other peripherals.

2.2. Gimbal controlled camera

A monocular IR camera, as shown in Fig. 4 from Point Grey GS3-U3-41C6NIR is employed to track the IR-LED lightened marker. The camera is able to provide 2048×2048 resolution grey image with relatively high quantum efficiency at 850 nm wavelength. The IR-LEDs mounted below the transparent marker emit IR light to indicate its location and also facilitate the visibility during the night. However, the light is generally invisible to human eyes. The visual marker is placed on top of the vehicle, so the camera is required to point directly downwards. To stabilize and to control the angle of the camera, the Arris Zhaoyun Brushless Gimbal is adopted for the work.

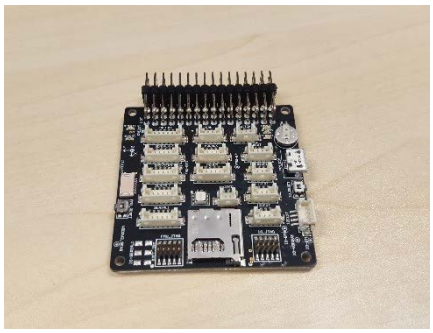

Fig. 3. Self-customized flight controller for T-Lion UAV.

Fig. 4. Point Grey IR camera with a 3D printed adapter.

3. UAV Dynamics Model Identification

To achieve good tracking performance, mathematical model of T-Lion is first identified. Most of the literature work on quadrotor UAV modelling and control are based on linear model [22]. However, in order to study the dynamics of the UAV in a high-speed tracking motion, linearized model might not be sufficient. In this manuscript, a nonlinear multi-rotor UAV mathematical model will be derived, then followed by an inverse dynamic linearization approach to allow linear controllers to be designed on the system.

In the last decade, nonlinear UAV model, especially multi-rotor UAV, has been developed and extensively revised by many research institutes [23-25]. A major difference between the derived models from different researchers is the assignment of the initial frame and the body frame. In this manuscript, we follow the standard practice of having a fixed origin frame (also called a ground frame) as initial frame, and a moving frame (also called a body frame) that is attached at the center of gravity (CG) of the UAV. The frame assignment follows what was documented in [26].

In this convention, the origin frame is commonly be referred as the North-East-Down (NED) frame, where the x, y, and z axes point towards the actual North, East and downwards direction of the Earth, respectively. The origin of the frame is fixed relative to the Earth, where it is chosen to be at the point where the UAV is powered up. On the other hand, the origin of the body frame is located at the CG of the multi-rotor UAV, with x, y, and z axes point towards the front, left, and

down direction of the UAV, respectively. This frame is fixed on the UAV's fuselage and will move linearly and circularly along with the UAV.

With these frames' assignment, the derivation of the nonlinear mathematical model of the multi-rotor UAV is derived as shown in the subsections below.

3.1. Non-linear model overview

The model overview and the signal flow of the quadrotor UAV is shown in Fig. 5. In this block diagram, the inputs to the UAV, δ_n, shown at the beginning of the block diagram, are the normalized PWM control signals sent from the flight controller board. The linear velocity $\boldsymbol{V_b} = (u, v, w)^T$, linear position $\boldsymbol{P_n} = (x, y, z)^T$, Euler angle $\boldsymbol{\theta} = (\phi, \theta, \psi)^T$, and angular velocity $\boldsymbol{\omega} = (p, q, r)^T$ shown on the end of the block diagram are the output of the system, which will be used on feedback control later. Note that in the following derivation, the quadrotor UAV are designed to be in cross X configuration, with rotor number 1, 2, 3, and 4, each corresponds to front-right, back-left, front-left, and back-right positions.

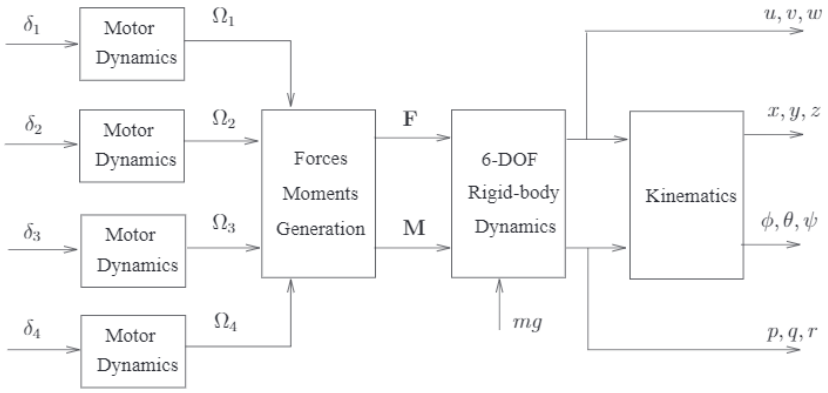

Fig. 5. Overview signal flow of the quadrotor UAV mathematical model.

3.2. Kinematics and rigid-body dynamics

The motions between the NED and the body frame can be related with two well-known navigation equations. They are shown here for completeness and will not be further discussed. Interested readers can refer to [26] for derivations of these equations.

$$\dot{P}_n = R_{n/b} V_b, \tag{1}$$

$$\dot{\theta} = S^{-1} \omega, \tag{2}$$

where the rotational matrix, $R_{n/b}$, and the lumped transformation matrix, S^{-1}, are given by

$$R_{n/b} = \begin{bmatrix} c_\theta c_\psi & s_\phi s_\theta c_\psi - c_\phi s_\psi & c_\phi s_\theta c_\psi + s_\phi s_\psi \\ c_\theta s_\psi & s_\phi s_\theta s_\psi + c_\phi c_\psi & c_\phi s_\theta s_\psi - s_\phi c_\psi \\ -s_\theta & s_\phi c_\theta & c_\phi c_\theta \end{bmatrix}, \tag{3}$$

$$S^{-1} = \begin{bmatrix} 1 & s_\phi t_\theta & c_\phi t_\theta \\ 0 & c_\phi & -s_\phi \\ 0 & s_\phi/c_\theta & c_\phi/c_\theta \end{bmatrix}, \tag{4}$$

with $s_* = \sin(*)$, $c_* = \cos(*)$, and $t_* = \tan(*)$.

To describe the motions of any rigid-body, any motions can be estimated with Newton-Euler equations, that is:

$$m\dot{V}_b + \omega \times (mV_b) = F, \tag{5}$$

$$J\dot{\omega} + \omega \times (J\omega) = M, \tag{6}$$

where F and M are the force and moment vectors acting on the body. As the designed UAV is four ways symmetrical, the inertia matrix, J, is assumed to be diagonal, i.e.,

$$J = \begin{bmatrix} J_x & 0 & 0 \\ 0 & J_y & 0 \\ 0 & 0 & J_z \end{bmatrix}. \tag{7}$$

3.3. Forces and moments

The main quadrotor UAV movements are contributed by the forces and moments generated by itself, and also the external forces and moments acting on the fuselage. In general, there are 3 main sources as mentioned in [27, 28], i.e., the gravitational force, the rotor thrust and moment, and the fuselage drag force due to air movement. In the derivation shown in this manuscript, as there is no way to measure the velocity of wind, the ground speed is approximated as the air speed of the UAV.

First, the gravitational force applied directly downwards towards the Earth, which is along positive z-axis of the proposed NED frame. By transforming it to the body frame, we have

$$F_{gravity} = {R_{n/b}}^{-1} \begin{bmatrix} 0 \\ 0 \\ mg \end{bmatrix} = \begin{bmatrix} -mgs_\theta \\ mgc_\theta s_\phi \\ mgc_\theta c_\phi \end{bmatrix}. \tag{8}$$

Forces and moments generated by the UAV mainly come from the rotors. Due to the small rotor size, and the rigidity of the rotor, the flapping dynamics are not considered in this work. Thus, we can safely assume each rotating rotor creates a thrust, T_n, and a moment, Q_n, for $n = 1,2,3,4$ along their axes. From the aerodynamics consideration, the thrust and torques produced are modelled as

$$T_n = \frac{1}{4\pi^2} C_T \rho (2r)^4 \Omega_n^2, \tag{9}$$

$$Q_n = \frac{1}{4\pi^2} C_Q \rho (2r)^5 \Omega_n^2. \tag{10}$$

Here, C_T and C_Q are the aerodynamic coefficients of the propeller, ρ is the density of the air, r is the radius of the rotor blade. As the collective pitch angle of the propeller is fixed in this work, the aerodynamic coefficients are assumed to be constants. As the density of air, and the radius of rotor blade are also unchanged at low altitude flight, Eqs. (9) and (10) can be simplified to

$$T_n = k_T \Omega_n^2, \tag{11}$$

$$Q_n = k_Q \Omega_n^2, \tag{12}$$

where the constants k_T and k_Q to be estimated through bench experiments.

The total thrusts and moments of the quadrotor UAV due to the rotations of the four motors are derived as:

$$F_{rotor} = \begin{bmatrix} 0 \\ 0 \\ -(T_1 + T_2 + T_3 + T_4) \end{bmatrix}, \tag{13}$$

$$M_{rotor} = \begin{bmatrix} \frac{\sqrt{2}}{2} l(T_2 + T_3 - T_1 - T_4) \\ \frac{\sqrt{2}}{2} l(T_1 + T_2 - T_3 - T_4) \\ Q_1 + Q_3 - Q_2 - Q_4 \end{bmatrix}. \tag{14}$$

In this research work, an acceptable performance of the UAV travels at a high velocity (10 m/s) needs to be guaranteed, due to the tracking of the ground vehicle. Thus, the drag force due to air resistance needs to be modelled. We formulate the drag force as directly proportionate to the air speed, which is valid in the operating speed of the UAV (below 10 m/s).

$$F_{drag} = \begin{bmatrix} -b_w & 0 & 0 \\ 0 & -b_w & 0 \\ 0 & 0 & 0 \end{bmatrix} V_b, \tag{15}$$

where b_w is the drag coefficient. The coefficient can be identified using a wind tunnel.

3.4. D.C. motor dynamics

An electric motor is a second order system due to its electrical and mechanical dynamics. It is generally sufficient to assume that the motor is a first order system, as the electrical dynamic is generally much faster than the mechanical dynamic [29]. In this case, the motor dynamics is modelled as

$$\dot{\Omega}_n = \frac{1}{\tau_m} [k_m(\delta_n - \delta_n^*) - \Omega_n]. \tag{16}$$

Here, the Ω_n is the motor rotating speed, k_m is the steady state gain, τ_m is the time constant, and δ_n^* is the normalized input trim where the motor starts spinning. Please note that δ_n is the normalized input to the electronic speed controller (ESC), with the following normalization process,

$$\delta_n = \frac{u_n - 1000}{1000}, \tag{17}$$

where u_n is the PWM signal fed to the electronic speed controller in unit μs. In general, the pulse widths to the ESC are limited at minimum of 544 µs and maximum of 2400 µs.

3.5. Parameters identification

There are several parameters in the derived mathematical model from Eqs. (1) to (17) that need to be identified. Table 1 shows the list of parameters to be identified.

Table 1. UAV Parameters to be Identified.

Parameter	Unit	Physical Meaning
g	ms^{-2}	Gravity acceleration
m	kg	Mass of quadrotor
l	m	Length of rotor arm
k_T	$\mathrm{N\ rad}^{-2}$	Rotor thrust coefficient
k_Q	$\mathrm{Nm\ rad}^{-2}$	Rotor torque coefficient
k_m	-	Steady-state gain of D.C. motor
τ_m	s	Time constant of D.C. motor
J_x	kgm^2	Moment of inertia at x-axis
J_y	kgm^2	Moment of inertia at y-axis
J_z	kgm^2	Moment of inertia at z-axis
b_w	-	Fuselage drag coefficient

Among the parameters, m and l can be directly measured from the UAV. They are respectively 4.2 kg and 0.303 m. Gravity acceleration is assumed to be 9.781 m/s² in Singapore. Moment of inertia of the multi-rotor UAV can be obtained via the tri-filar pendulum experiment introduced in [29]. The moment of inertia of the UAV is found to be

$$J = \begin{bmatrix} 0.10004 & 0 & 0 \\ 0 & 0.10369 & 0 \\ 0 & 0 & 0.14311 \end{bmatrix}. \tag{18}$$

To obtain aerodynamics coefficients, an experiment was conducted by placing the motor on a load cell which will measure thrust and torque produced by the motor, at the same time recording the rotating speed of the motor. The value of k_T and k_Q can be approximated by the gradient of the best fit curve between thrust/torque and rotating speed square,Ω^2. Figures 6 and 7 show the plots to find k_T and k_Q, respectively, where

$$k_T = 1.0795 \times 10^{-4}, \tag{19}$$

$$k_Q = 3.0140 \times 10^{-6}. \tag{20}$$

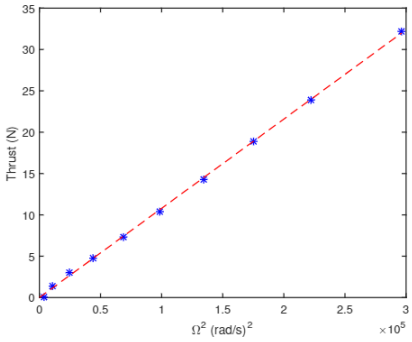

Fig. 6. Motor thrust against rotating speed squared.

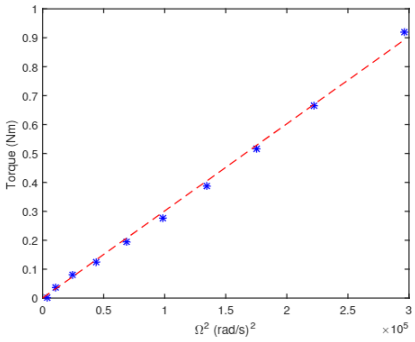

Fig. 7. Motor torque against rotating speed squared.

The motor steady-state gain k_m and time constant τ_m can also be obtained from the experiment described above. The gradient of steady-state rotating speed against normalized PWM input is approximated as $k_m = 557.1667$ while the time constant is obtained from 63.2% of the rise time as $\tau_m = 0.66$ s.

Lastly, to identify wind drag force coefficient b_w, a wind tunnel test on the UAV rotor was conducted. Five different wind speed at 0, 5, 10, 15 and 20 m/s were injected to the rotating rotor. The drag force along the wind axis is recorded for different wind speed and rotating speed with the load cell. b_w is obtained from the gradient of the best fit line of wind speed against thrust. It is noted that at different rotating speed, b_w is also different. Generally, as the rotating speed of the rotor increase, b_w will increase due to higher drag experienced by the blade. In our model, we adopt the value of b_w at 3000 RPM, in which the rotors at this speed provide exact thrust to lift the UAV. In this case, $b_w = -0.5324$.

4. Flight Controller Design

In this section, the detail design methodology of the flight controller is discussed. The dynamics of the quadrotor UAV as identified in the previous section can be expressed in the following forms:

$$\dot{V}_b = -\omega \times V_b + \frac{F_{gravity}}{m} + \frac{F_{drag}}{m} + \frac{F_{rotor}}{m}, \tag{21}$$

$$\dot{\omega} = -J^{-1}[\omega \times J\omega] + J^{-1}M_{rotor}. \tag{22}$$

Here, the input to the UAV system is exactly the forces and moments generated by the rotors, in this case, F_{rotor} and M_{rotor}. As m and J are constants that were identified in the previous section, we let

$$U_F = \frac{F_{rotor}}{m} = \begin{bmatrix} u_{Fx} \\ u_{Fy} \\ u_{Fz} \end{bmatrix}, \tag{23}$$

$$U_M = J^{-1}M_{rotor} = \begin{bmatrix} u_{Mx} \\ u_{My} \\ u_{Mz} \end{bmatrix}, \tag{24}$$

be the inputs to be controlled to the UAV system. As all other terms in Equation (21) and (22) can be measured or estimated as state-variables, a feedback linearized system can be obtained with

$$\bar{U}_F = U_F - \omega \times V_b + \frac{F_{gravity}}{m} + \frac{F_{drag}}{m}, \tag{25}$$

$$\bar{U}_M = U_M - J^{-1}[\omega \times J\omega]. \tag{26}$$

The linearized UAV position and orientation dynamics are reduced to simple forms

$$\dot{V}_b = \bar{U}_F = \begin{bmatrix} \bar{u}_{Fx} \\ \bar{u}_{Fy} \\ \bar{u}_{Fz} \end{bmatrix}, \tag{27}$$

$$\dot{\omega} = \bar{U}_M = \begin{bmatrix} \bar{u}_{Mx} \\ \bar{u}_{My} \\ \bar{u}_{Mz} \end{bmatrix}. \tag{28}$$

Noted here that there are a total of 6 motions for the UAV in 3D space, with 3 translational motions, and 3 rotational motions. However, there are only four degree-of-freedom (DoF) on the control channels of the quad-rotor UAV. Due to the facts that the rotors mounted on the multi-rotor UAV system is fixed on the fuselage and also has fixed pitch angle, the lateral motion on x and y axes are affected by the rotational motion on these axes, respectively. Their relationships can be approximated as the following equations:

$$a_x \approx g\theta, \tag{29}$$

$$a_y \approx g\phi, \tag{30}$$

where $u_{Fx} = a_x$, $u_{Fy} = a_y$, $u_{Mx} = \ddot{\theta}$, and $u_{My} = \ddot{\phi}$. The approximation holds when the angles (θ, ϕ) is small. With this, the lateral movements on x and y direction will be reflected by controlling the rotating movement on these axes, respectively.

With this linearization approach, the UAV dynamics system has become linear in each axis. Individual orientation controller can be designed with rapid responses, then a position controller can be cascaded with slower responses. As the design of UAV linear flight controller has been extensively discussed in the literature (refers to [22], [29-31]), it will not be repeated in this manuscript.

5. Target Position Estimation

Besides the flight controller designed to facilitate tracking performance of the UAV, another core of the research lies on the relative position estimation of the UAV and the moving platform with pre-designed marker.

Common measurement devices are the IMU, GPS, 2D or 3D laser scanner, radar, and camera. To simulate actual application of this system working in unstable GPS reception, GPS is not used in the position computation of the UAV. In fact, in the progress of this research development, vision system was first used to estimate all x-, y-, and z- position of the UAV. However, it was found that the solution with vision system alone cannot provide an accurate depth (in this case, z-position of the UAV) estimation. As the accuracy of depth measurement is important to be used in x- and y-position estimation, a laser scanning range finder will be utilized to robustly obtain the flying height of the UAV.

5.1. Height estimation

An accurate height measurement, with at least up to the centimetre scale, is essential for precise landing on the moving target, and to better estimate the x- and y-position of the UAV relative to the moving target. A good height measurement allows the UAV to perform autonomous take-off and landing from a moving target with more robustness. To achieve this, a 2D scanning laser range finder with resolution of millimetres accuracy is utilized and installed on-board of T-Lion. An intelligent algorithm to estimate the UAV height via its range measurements is developed and will be explained in this subsection.

In our solution, a Hokuyo laser range finder is utilized. It has 1081 output values representing the measured distances in millimetre from the scanner to its surrounding, in a 270 degrees field-of-view. As the data obtained is in polar

coordinates (r_i, θ_i), a simple transformation can be applied to convert it to Cartesian coordinates (x_i, y_i) by

$$x_i = r_i \cos \theta_i, \tag{31}$$

$$y_i = r_i \sin \theta_i. \tag{32}$$

The obtained data then consists of 1081 points of features in x and y coordinate. These data include a lot of unwanted noise and out-of-range measurement, which needed to be filtered. To filter the data, a split-and-merge (SAM) algorithm is proposed. This algorithm will classify the raw data into a cluster of points that can be identified as line segments. Any points that fall out of the line segments are considered as outliers and will not be taken into account. The main steps of the proposed SAM algorithm are summarized below.

i. The first point (A) and the last point (B) of the raw data is identified. A straight line is generated using these two points.

ii. Calculate the shortest distance (perpendicular distance) of all other points along AB. The largest distance from any point is identified, and the point is noted as C.

iii. If the distance C to line AB is well within a threshold value, which can be changed as a designing parameter, then a cluster is created by joining a straight line from A to C, and another straight line from C to B.

iv. The SAM algorithm (step 1) is recursively run on each cluster (e.g.: A-C and C-B cluster). It will only stop when all threshold values are not met.

v. The end results of the SAM algorithm will be straight lines with different angles representing each useful segment of the scanned objects.

Figure 8 shows the graphical illustration of the SAM algorithm for visual understanding. Upon the end of SAM algorithm, clusters of lines are created. Each line is represented by the line's normal direction α_k and its perpendicular distance to the source of laser scanner d_k, as shown in the final form in Fig. 8.

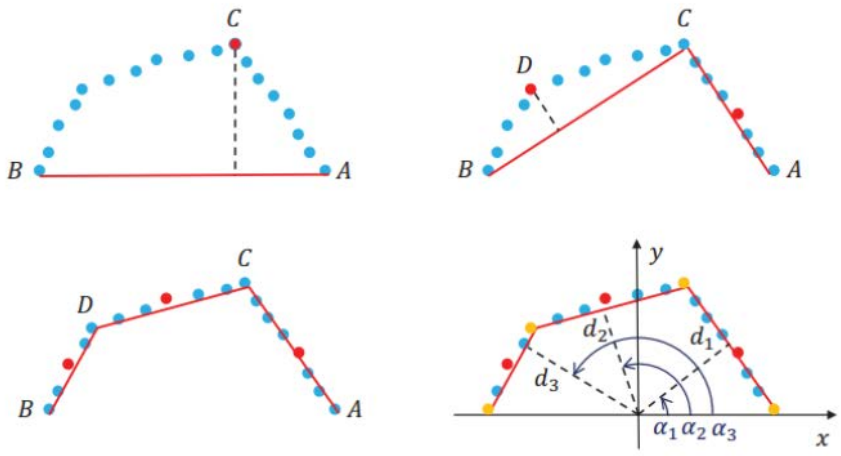

Fig. 8. Steps on split-and-merge algorithm.

The next step is to identify lines that are parallel to ground level. This step will further filter out line segments that is not belonging to the ground, which are not in our interests. Since the obtained lines are still expressed in the laser scanner frame, their directions α_k should be compensated by the UAV roll angle ϕ and then compare to the normal line of the ground plane which is at $\pi/2$. We then have

$$\Delta\alpha_k = \alpha_k - \phi - \pi/2. \quad (33)$$

Here, the value of $\Delta\alpha_k$ is the angle between the actual ground plane, and the identified line. Due to the nature of environment, some ground plane is slightly slanted. In this case, a threshold value is set as 5 degrees. All other lines that do not fall within the 5 degrees range is filtered. Finally, the remaining lines are sorted by their perpendicular distances to the UAV and the furthest ones are kept. Among them, the longest line is believed to be the true ground.

Once the true ground is identified, the perpendicular distance of this line to the laser scanner source is compensated with the UAV pitch angle θ and the offset between the laser scanner and the UAV center of gravity, Δh, leaving the final height estimation to be

$$h = r\cos\theta - \Delta h. \quad (34)$$

Figure 9 shows the flow of the laser scanner height estimation algorithm. This method ensures that the actual flying height of the UAV can be obtained, as long as part of the laser range scanner ray project to the actual ground.

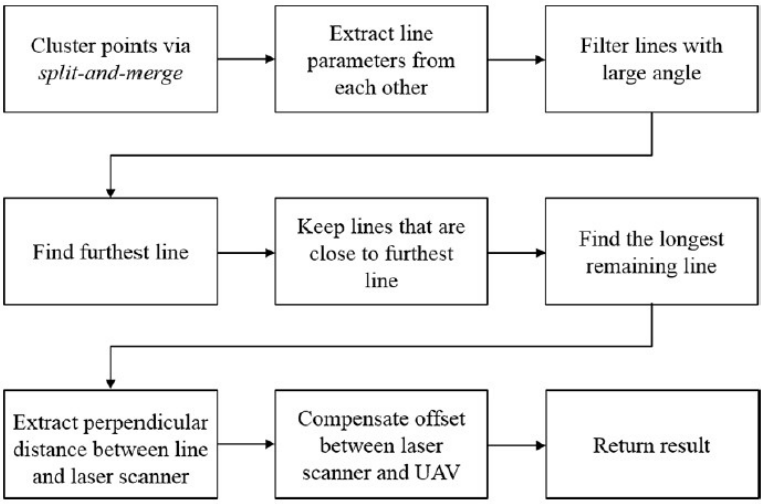

Fig. 9. Steps to compute height via laser range sensor.

5.2. Vision-based position estimation

With a robust and accurate depth estimation, a vision-based localization system is developed for the task of landing on the moving ground vehicle. This algorithm will provide relative distance estimation between the UAV and the moving target in x- and y-directions. This information is further used for automatic landing on the target.

The visual target is customized with a specially designed marker, where it differs from most natural landmarks. The designed marker is in the form of cascaded AprilTag marker visualized in Fig. 10. The steps of the proposed vision localization system are to first identify the correct target in the captured image, and then to estimate the 3D position of the actual target on the moving vehicle.

Fig. 10. Cascaded Apriltag marker design.

The original AprilTag visual fiducial algorithm documented in [32] could run at 5 Hz speed on Intel i7 Quad-core processor, which is not suitable for real-time processing for UAV control. Optimization and improvement of the open-source algorithm was performed by replacing most of the functions in the algorithm to the more optimized OpenCV functions. As a result, the improved AprilTag algorithm could run at around 18 Hz with image resolution of 640×480. It has an effective range from ground to 18 m in the air which is suitable for real-time implementation on-board the UAV [33]. Figure 11 elaborates the flow of the algorithm. The improvement came with a trade-off with lower accuracy, which will be shown and discussed in Section 6 later.

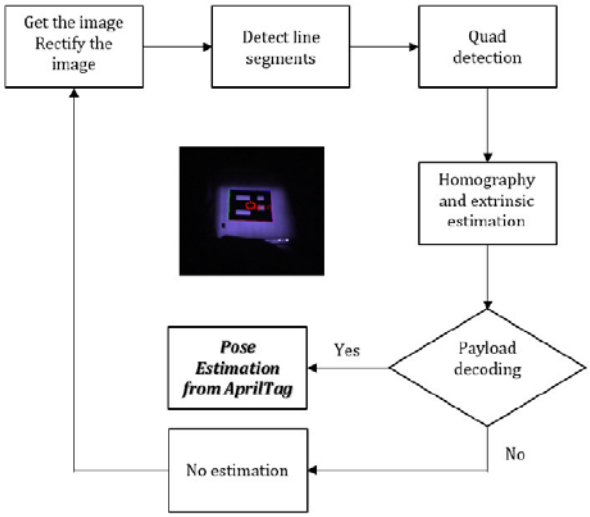

Fig. 11. Flow diagram of apriltag detection algorithm.

In our implementation, we used a 1.2 m by 1.2 m IR-LED illuminated marker to localize our UAV with respect to the ground moving vehicle. The LED is not visible by naked eyes, but it is well lid from the IR images captured by the aforementioned IR camera. This enables the system to work even at ultra-low illumination condition, such as during nighttime without streetlight, while remain hidden from human eyes.

5.3. Benchmarking results

The pose estimation algorithm mentioned above was implemented on T-Lion. A piloted flight test was conducted in a controlled environment with VICON setup for benchmarking purpose. VICON motion tracking system is able to provide 3D coordinate of objects in real time at 200 Hz. It is widely used in filming industry where human or animal movement can be modelled precisely in terms of millimetre accuracy.

In the experiment setup, UAV is commanded to fly randomly in an oscillation manner. Position estimated from both VICON system, and the on-board vision-laser system are logged and compared. Figure 12 shows both the position estimations plotted in the same axis. In red, measurement from VICON system provides position estimation up to mm scale accuracy. On the other hand, position estimated using vision-laser sensor (blue line) provides us a good estimation with a very close result to VICON system.

6. System Simulation and Actual Flight Trials Results

To verify the proposed methodology, first a simulated environment has been constructed in MATLAB. Upon positive results obtained from MATLAB simulation, an actual UAV is built, and the target tracking and landing capabilities are implemented. Actual flight trials were conducted on a straight path of road, with the UAV is commanded to track a moving truck at 10 m/s speed, and then commanded to land on the truck. Both the simulation and the implementation results are shown in this section.

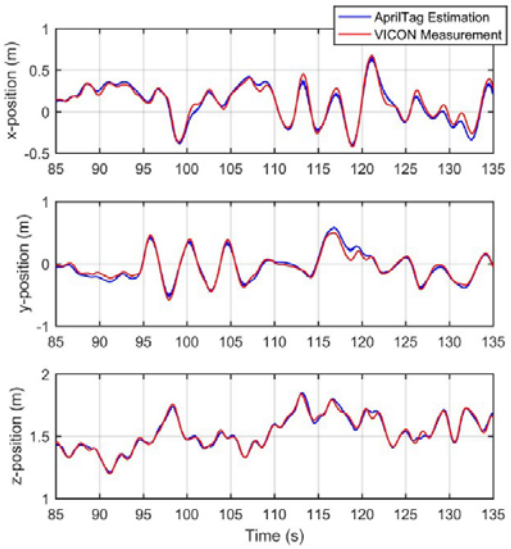

Fig. 12. Performance of the proposed pose estimation compared to VICON motion tracking results.

6.1. Full systems simulation

The simulation of the system was done in MATLAB environment, with the following dynamics included in the simulated system:

i. Dynamics of the moving vehicle is modelled based on a 4-wheel ground vehicle, with front wheels steer control. The vehicle acceleration is limited to 1 m/s², to start from 0 m/s speed up to 10 m/s speed (36 km/h).

ii. Detection of the moving vehicle from the UAV is simulated as the difference between their positions, with a 5% noise added in, along with 50 ms (approximately 18 Hz) delay, which is in line with the accuracy and speed of the improved AprilTag detection algorithm developed for this project.

iii. Quad-rotor UAV is modelled according to the model provided in Section 3. In addition, wind tunnel data on high airspeed manoeuvring was also used to determine drag force of the UAV in high-speed flying.

The simulation started with the UAV hovering at 4 m above the ground vehicle in static for 20 seconds, then the ground vehicle will start to accelerate to a linear speed of 10 m/s while the UAV will track and follow. At time $t = 30$ s, the UAV is commanded to land on it while it is still moving at a constant speed. Simulation ends when time $t = 60$ s has reached. Figure 13 shows the trajectory of the UAV and ground vehicle in the simulation for the whole duration of 60 s. The ground vehicle is observed to have moved approximately 350 m from the starting location.

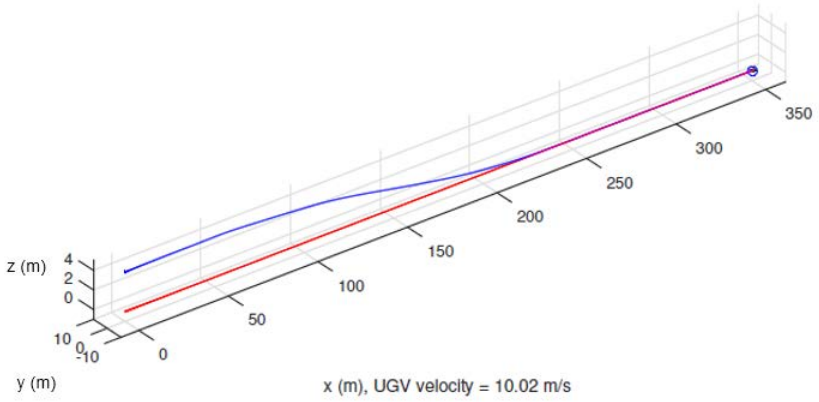

Fig. 13. Simulation on landing of the UAV on a moving platform, where the red line is the moving platform on ground, while the blue curve is the UAV trajectory while tracking and landing at the same time.

Figures 14 and 15 respectively shows the relative position between the UAV and the detected AprilTag, and the Euler angle (Roll and Pitch) of the UAV throughout the simulation. It is observed from the relative x-position error graph that an overshoot of approximately 1.25 m occurs when the ground vehicle starts to accelerate from 0 m/s to 10 m/s, then the overshot decreased rapidly then the ground vehicle decelerates upon reaching the maximum speed of 10 m/s. In the latter graph, it is also observed that the UAV pitched forward when the ground vehicle starts to move forward too, until a steady state of about -9 degree is reached, which corresponds to the pitch angle of the UAV to travel at 10 m/s speed.

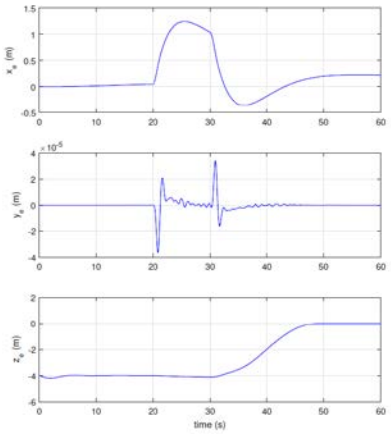

Fig. 14. Relative position estimated by the improved apriltag algorithm in the simulation

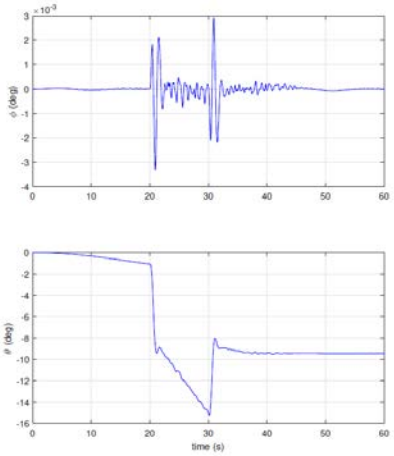

Fig. 15. Roll and pitch angle of the UAV during the tracking and landing process in the simulation.

6.2. Actual flight trials results

As the design concepts were proven in the simulation discussed above, the UAV is assembled, and actual flying tests were carried out to land the UAV on a moving truck.

The setup of the experiment can be visualized in Fig. 16, where a truck is manually driven by a driver on a straight path of approximately 300 m. In the experiment, the UAV will start its autonomous tracking and localization above the truck, where the IR illuminated AprilTag marker was placed at the back of the truck.

Fig. 16. Flight trials to autonomously track and land on a moving truck installed with the designed marker.

The results of the flight trial are plotted in Figs. 17 and 18. At time $t = 638$ s, the truck was slowly accelerated along the road to reach the maximum speed of 36 km/h (approximately 10 m/s). It can be observed in Fig. 17 that an overshoot of approximately 1.5 m occurred when the truck is accelerating forward. This Behavior matched rather well to our simulated data discussed in the earlier section.

At time $t = 650$ s, the UAV was commanded to land on the truck while it was still moving at 36 km/h speed. Again, similar behavior on z-axis relative position can be related on both simulation and actual flying data. In Fig. 18, the pitch angle of the UAV underwent similar trend as shown in the simulated result, with a forward pitching angle of approximate -9 degree in average can be observed. A sequence of the images of the landing that was captured by an on-board camera are shown in Fig. 19. Note that the images are infrared images.

In terms of detection success rate, each of the image frame captured by the on-board camera was analysed with the proposed improved AprilTag detection algorithm. In this case, two stages of the operation are analysed:

i. Static: the marker is static on the ground, while the UAV is 4 m above it;
ii. Dynamic: the marker moves in a constant velocity, while the UAV begins to land on the marker, from a 4 m height.

The unsuccessful detection and the total number of frames for each stage mentioned above is identified and failure rates are tabulated in Table 2. As compared to the open source AprilTag algorithm from [32], the performance of the algorithm drops slightly but still within an acceptable rate as the frame rate has improved greatly from 5 Hz to 18 Hz with our UAV on-board computer. The main reason in the drop of performance is due to the down-sampling of the image from HD to 640×480 pixels.

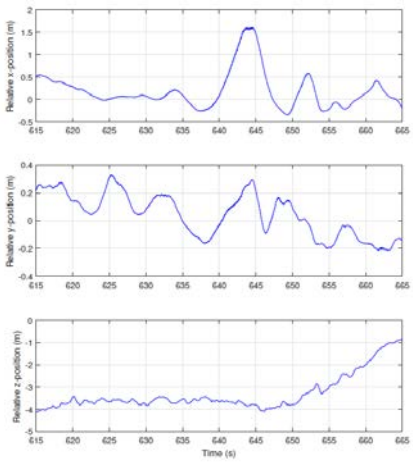

Fig. 17. Relative position estimated by the improved AprilTag algorithm in the actual flight trials.

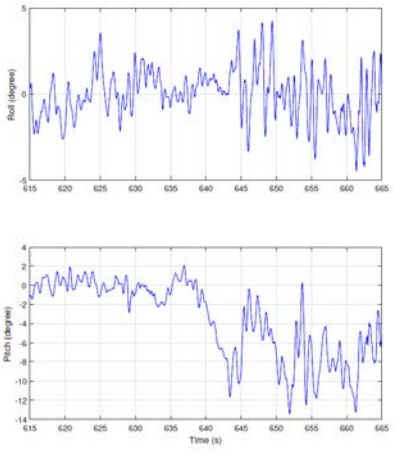

Fig. 18. Roll and pitch angle of the UAV during the tracking and landing in the actual flight trials.

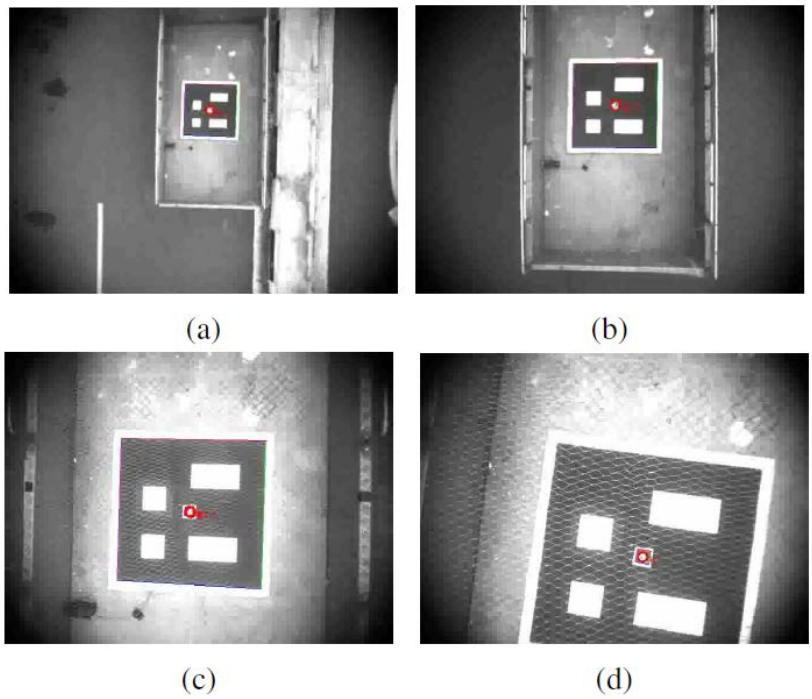

Fig. 19. Images sequence from on-board camera during landing: From (a) to (b), when the UAV is more than 2 m above the marker, only the large marker is detected; at (c), when the UAV is within 2 m, both large and small markers are detected; at (d), when the UAV is below 1 m, only the small marker is detected

Table 2. Error rate comparison between the improved AprilTag and the open-source AprilTag algorithms.

Error Rate	Improved Algo.	Open Algo. [30]
Static Marker	0.832%	0.469%
Dynamics Marker	5.593%	No Data Given
Frame Rate	18 Hz	5 Hz

7. Conclusions

In this manuscript, a system on autonomous landing of multi-rotor UAV on fast moving vehicle is proposed and discussed. The hardware selection and integration are first discussed. In particular for a loose-less tracking performance, an IR camera is employed to track the customized IR-lighted marker, allowing operation in both day and night condition. An improved AprilTag marker detection algorithm is proposed based on open-source software, to enable real-time high-speed marker detection. Then, mathematical model of the quad-copter including kinematics and dynamics as well as motor dynamics are derived. The corresponding flight controller based on multi-layer linearized integrator model is designed to achieve good tracking performance. The real flight experiment and MATLAB simulations are both conducted to validate the system design.

Acknowledgement

This project was financially supported by Research Program No. 9013103831 from Temasek Laboratories, the National University of Singapore.

References

1. Rajendran, R.; and Smith, H. (2018). Sensitivity analysis of design parameters of a small solar-powered electric unmanned aerial vehicle. *Journal of Engineering Science and Technology* (*JESTEC)*, 13(12), 3922-3931.
2. Sahwee, Z.; Mahmood, A.S.; Rahman, N.A.; and Sahari, K.S.M. (2017). Wind tunnel evaluation for control transition from elevator to stabilator of small UAV. *Journal of Engineering Science and Technology* (*JESTEC*), 12(6), 1617-1626.
3. Kendoul, F. (2012). Survey of advances in guidance, navigation, and control of unmanned rotorcraft system. *Journal of Field Robotics*, 29(2), 315-378.
4. Benbassat, D.; and Abramson, C. (2002). Landing flare accident reports and pilot perception analysis. *International Journal of Aviation Psychology*, 12(2) 137-152.
5. Belton, D.; Butcher, S.; Foulkes-Jones, G.; and Blanda, J. (1999). Helicopter recovery to a moving platform using a GPS relative positioning system. *Proceedings of the 12th International Technical Meeting of the Satellite Division of the Institute of Navigation*, 1769-1776.
6. Wang, F.; Liu, P.; Zhao, S.; Chen, B.M.; Phang, S.K.; Lai, S.; Pang, T.; Wang, B.; Cai, C.; and Lee, T.H. (2015). Development of an unmanned helicopter for vertical replenishment. *Unmanned Systems*, 3(1), 63-87.
7. Pervan, B.; Chan, F.; and Colby, G. (2003). Performance analysis of carrier-phase DGPS navigation for shipboard landing of aircraft, *Navigation*, 50(3), 181-191.
8. Hu, B.; Lu, L.; and Mishra, S. (2018) A control architecture for time-optimal landing of a quadrotor onto a moving platform. *Asian Journal of Control*, 20(5), 1701-1712.
9. Garratt, M.; Pota, H.; Lambert, A.; Eckersley-Maslin, S.; and Farabet, C. (2009). Visual tracking and lidar relative positioning for automated launch and recovery of an unmanned rotorcraft from ships at sea. *Naval Engineers Journal*, 121(2), 99-110.
10. Wang, K.; Phang, S.K.; Ke, Y.; Chen, X.; Gong, K.; and Chen, B.M. (2017). Vision-aided tracking of a moving ground vehicle with a hybrid UAV. *IEEE International Conference on Control and Automation.* Ohrid, Macadonia, 28-33.
11. Ho, H.W.; and Chu, Q.P. (2013). Automatic landing system of a quadrotor UAV using visual servoing. *In Proceedings of the Eurognc 2013, 2nd CEAS Specialist Conference on Guidance, Navigation and Control*. 1264-1283.
12. Yang, T.; Li, G.; Li, J.; Zhang, Y.; Zhang, X.; Zhang, Z.; and Li, Z. (2016). A ground-based near infrared camera array system for UAV auto-landing in GPS-denied environment. *Sensors*, 16(9), 1393.
13. Shakernia, O.; Vidal, R.; Sharp, C.S.; Ma, Y.; and Sastry, S. (2002). Multiple view motion estimation and control for landing an unmanned aerial vehicle. *IEEE International Conference on Robotics and Automation*, 2793-2798.
14. Zhang, L.; Deng, F.; Chen, J.; Bi, Y.; Phang, S.K.; Chen, X.; and Chen, B.M. (2018). Vision-based target three-dimensional geolocation using unmanned aerial vehicles. *IEEE Transactions on Industrial Electronics*, 65(10), 8052-8062.

15. Lange, S.; Sunderhauf, N.; and Protzel, P. (2009). A vision based onboard approach for landing and position control of an autonomous multirotor UAV in GPS-denied environments. *International Conference on Advanced Robotics*, 1-6.
16. Laiacker, M.; Kondak, K.; Schwarzbach, M.; and Muskardin, T. (2013). Vision aided automatic landing system for fixed wing UAV. *IEEE International Conference on Intelligent Robots and Systems*, 2971-2976.
17. Asl, H.J.; and Yoon, J. (2017). Bounded-input control of the quadrotor unmanned aerial vehicle: A vision-based approach. *Asian Journal of Control*, 19(3), 840-855.
18. Herisse, B.; Russotto, F.X.; Hamel, T.; and Mahony, R. (2008). Hovering flight and vertical landing control of a VTOL unmanned aerial vehicle using optical flow. *IEEE International Conference on Intelligent Robots and Systems*, 801-806.
19. Herisse, B.; Hamel, T.; Mahony, R.; and Russotto, F.X. (2009). A nonlinear terrain-following controller for a VTOL unmanned aerial vehicle using translational optical flow. *IEEE International Conference on Intelligent Robots and Systems*, 3251-3257.
20. Herisse, B.; Hamel, T.; Mahony, R.; and Russotto, F.X. (2010). The landing problem of a VTOL unmanned aerial vehicle on a moving platform using optical flow. *IEEE International Conference on Intelligent Robots and Systems*, 1600-1605.
21. Meier, L.; Tanskanen, P.; Heng, L.; Lee, G.H.; Fraundorfer, F.; and Pollefeys, M. (2012). PIXHAWK: A micro aerial vehicle design for autonomous flight using onboard computer vision. *Autonomous Robots*, 33(1-2), 21-39.
22. Mellinger, D.; and Kumar, V. (2011). Minimum snap trajectory generation and control for quadrotors. *2011 IEEE International Conference on Robotics and Automation (ICRA).* Shanghai, China, 2520-2525.
23. Bresciani, T. (2008). *Modelling, identification and control of a quadrotor helicopter*. Master. Thesis. Lund University, Lund, Sweden.
24. Raffo, G.V.; Ortega, M.G.; and Rubio, F.R. (2010). An integral predictive/nonlinear H-infinity control structure for a quadrotor helicopter. *Automatica*, 46(1), 29-39.
25. Wardihani, E.D.; Ramdhani, M.; Suharjono, A;, Setyawan, T.A.; Hidayat, S.S.; Helmy; Widodo, S.; Triyono, E.; and Saifullah, F. (2018). Real-time forest fire monitoring system using unmanned aerial vehicle. *Journal of Engineering Science and Technology* (*JESTEC*), 13(6), 1587-1594.
26. Cai, G.; Chen, B.M.; and Lee, T.H. (2011). *Unmanned rotorcraft systems*. London/New York: Springer
27. Goel, R.; Shah, S.M.; Gupta, N.K.; and Ananthkrishnan, N. (2009). Modeling, simulation and flight testing of an autonomous quadrotor. *Proceedings of International Conference on Environmental and Agriculture Engineering*. Bangalore, India.
28. Bouabdallah, S.; Murrieri, P.; and Siegwart, R. (2004). Design and control of an indoor micro quadrotor. *IEEE International Conference on Robotics and Automation.* New Orleans, USA, 4393-4398.
29. Phang, S.K.; Li, K.; Yu, K.H.; Chen, B.M.; and Lee, T.H. (2014). Systematic design and implementation of a micro unmanned quadrotor system. *Unmanned Systems*, 2(2), 121-141.

30. Chen, B.M.; Lee, T.H.; and Venkataramanan, V. (2002). *Hard disk drive servo systems*. Springer Berlin.
31. Chen, B.M. (2013). *Robust and H-infinity Control*. Springer Science and Business Media.
32. Olson, E. (2011). AprilTag: A robust and flexible visual fiducial system. *Proceedings of the IEEE International Conference on Robotics and Automation*. 3400-3407.
33. Chen, X.; Phang, S.K.; and Chen, B.M. (2017). System integration of a vision-guided UAV for autonomous tracking on moving platform in low illumination condition, *Proceedings of the ION Pacific PNT 2017 Conference*. Hawaii, US, 1082-1092.